



ELSEVIER

Thin-Walled Structures •• (2001) ••–••

THIN-WALLED  
STRUCTURES

www.elsevier.com/locate/tws

## Nonlinear response of shell structures: effects of plasticity modelling and large rotations

B. Skallerud <sup>a,\*</sup>, L.I. Myklebust <sup>a</sup>, B. Haugen <sup>b</sup>

<sup>a</sup> Faculty of Mechanical Engineering, Div. Applied Mechanics, The Norwegian University of Science and Technology, K Hejesvei 2, N-7491, Trondheim, Norway

<sup>b</sup> FEDEM Technology a.s., N 7030, Trondheim, Norway

Received 29 August 2000; accepted 19 March 2001

### Abstract

Many structural applications require nonlinear finite element analyses in order to assess response and capacity. Plastic deformations may be accounted for by means of thickness integration or stress resultants. The stress resultant model employed herein is based on Ilyushins' linear yield criterion for thin shells. The corners present with this criterion are circumvented by means of a simplification, hence, there is no need for multi-surface stress resultant updates. A backward Euler difference is employed in the stress resultant update, and a consistent tangent is used in the Newton–Raphson iterations on the global equilibrium. Limit points are traversed by means of an orthogonal trajectory method. The response of compression dominated shells with imperfections typically corresponds to limit point behaviour. For stress resultant plasticity, the nonlinear transition from initial yield to full plasticity in shell bending is missed. Hence, the efficiency obtained by eliminating thickness integration is countered by some inaccuracy in the response simulation. This is investigated by means of comparison with finite element simulations employing integration through thickness (with linear or nonlinear hardening). Both steel and aluminium alloys are considered. In collapse response of slender structures, the straining of the material may be moderate, but the motion may be governed by large rigid body translations and rotations. A way of accounting for this by means of the co-rotated approach is presented. Triangular high-performance facet shell elements are employed. By example computations, the importance of nonlinear geometry contributions is illustrated. © 2001 Published by Elsevier Science Ltd.

*Keywords:* Plasticity modelling; Large rotations; Co-rotated formulation; Assumed strain thin shell finite element

\* Corresponding author. Tel.: + 47-73-59-3560; fax: +47-73-59-3491.

E-mail address: bjorn.skallerud@mtf.ntnu.no (B. Skallerud).

1  
2  
3  
69

**1. Introduction**

70  
71  
72  
73  
74  
75  
76  
77  
78  
79  
80  
81  
82  
83  
84  
85  
86  
87  
88  
89  
90  
91  
92  
93  
94  
95  
96  
97  
98  
99  
100  
101  
102  
103

Shell structures are used in many engineering applications due to efficient load carrying capability relative to material volume. Reassessment of the capacity of existing structures reaching their original service life, assessment of structural behaviour during damage scenarios, and residual (post-damage) analyses typically require calculations accounting for nonlinear behaviour. For shell structures computations are carried out by means of shell finite elements. In many cases the nonlinear deformations of the shell are governed by large rigid body translations and rotations, and moderate strain producing motions. This simplifies the constitutive modelling. The use of rotational degrees of freedom at the shell element nodes needs special consideration for large spatial rotations. In the present study the co-rotated formulation is employed [1–6]. With this, the strain producing deformations and the (large) rigid body motion is split, and simplifications in strain description are easily carried out with respect to the co-rotated system. Herein a triangular assumed natural deviatoric strain shell finite element (ANDES) presented by Felippa et al. is used [7,8]. This is a non-conform element satisfying the individual element test [9]. Plasticity is accounted for either by means of integration of stress over the thickness (layer approach), or stress resultants modelling. By the latter approach the yield surfaces become more complicated than in the former. For instance, a layer approach with Mises material (no discontinuities in the yield surface gradient in the plane stress space) corresponds to a stress resultant yield surface with corners (Ilyushin). This requires special considerations in the stress resultant update algorithm. In the present study this yield surface is simplified to a hyperellipse, avoiding the corners at the expense of introducing some inaccuracy in response calculation at inelastic integration points [10–12]. In [13] a stress resultant approach also was employed for determination of capacity of plates.

The main objectives with the present investigation are: 1) quantify the inaccuracy of the stress resultant approach, 2) indicate remedies for this, and 3) investigate the effects of large rotations (e.g. when is a rotation large?). The paper is organised as follows. First the shell kinematics are presented. This includes the co-rotated formulation and definition of the deformational (strain producing) degrees of freedom. Secondly, variation of the force equilibrium leads to the consistent tangent stiffness. The stress resultant update and its linearization are briefly presented. Finally, several examples of shell problems are analysed and compared to other published simulations. Additional simulations and discussions may be obtained from [11,12].

104

**2. Shell finite element kinematics**

105  
106  
107  
108

Fig. 1 shows the two basic coordinate systems that are used. The global coordinate system is represented by unit vectors  $I_1, I_2$  and  $I_3$ . The co-rotated element coordinate system shared by shadow configuration  $C_{0n}$  and configuration  $C_n$  is represented by unit vectors  $i''_1, i''_2$  and  $i''_3$ . Vectors given in the local co-rotated element coordinate

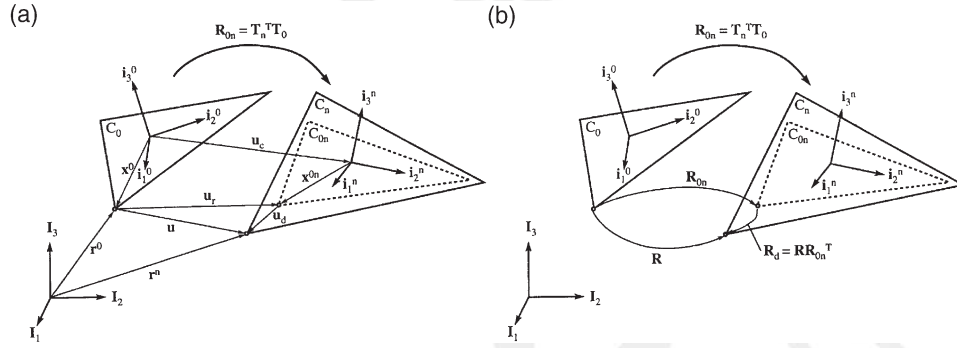


Fig. 1. Shell element kinematics, co-rotated approach.

system are marked with a tilde (~). A vector  $\mathbf{x}$  in global coordinates is transformed into a vector  $\tilde{\mathbf{x}}$  in the local coordinate system 0 by

$$\tilde{\mathbf{x}} = \mathbf{T}_0 \mathbf{x} \mathbf{T}_0 = \begin{bmatrix} \tilde{i}_1^{0T} \\ \tilde{i}_2^{0T} \\ \tilde{i}_3^{0T} \end{bmatrix} \quad (1)$$

$\mathbf{T}_0$  is orthonormal. The rigid body rotation of  $\tilde{i}_i^0$  to  $\tilde{i}_i^n$  is given by

$$\tilde{i}_1^n = \mathbf{R}_{0n} \tilde{i}_1^0 \mathbf{R}_{0n}^T = \mathbf{T}_n^T \mathbf{T}_0 \quad (2)$$

where  $\mathbf{R}_{0n}$  is the rigid body rotation matrix from position 0 to position  $n$ . The Rodrigues representation of the rotation matrix is used. The rotation matrix for a rotation  $\theta$  about an axis defined by the unit vector  $\mathbf{n}^T = [n_1 n_2 n_3]$  is written [14]:

$$\mathbf{R} = \mathbf{I} + \mathbf{N} \sin \theta + \mathbf{N}^2 (1 - \cos \theta) \quad (3)$$

$$\mathbf{N} = \mathbf{Spin}(\mathbf{n}) = \begin{bmatrix} 0 & -n_3 & n_2 \\ n_3 & 0 & -n_1 \\ -n_2 & n_1 & 0 \end{bmatrix} \quad (4)$$

$\mathbf{I}$  is the 3 by 3 identity matrix. Rotation of a vector  $\mathbf{r}_0$  into  $\mathbf{r}$  through an angle  $\theta$  about an axis defined by the unit vector  $\mathbf{n}$  is obtained by:

$$\mathbf{r} = \mathbf{R} \mathbf{r}_0 \quad (5)$$

1  
2  
3  
129  
130  
131  
133  
134  
135  
136  
138  
139  
140  
141  
142  
143  
146  
147  
148  
149  
150  
2  
152  
153  
154  
155  
156  
159  
160  
161  
162  
163  
165  
166  
167  
168  
169  
170  
171  
172  
173  
  
1  
2

Consider a body in initial configuration  $C_0$  moving to configuration  $C_n$ . The displacement vector is given as the difference between the position vector in configuration  $C_0$  and the position vector in configuration  $C_n$ .

$$\mathbf{u} = \mathbf{r}^n - \mathbf{r}^0 \tag{6}$$

The displacement vector is split into a deformational displacement vector and a rigid body displacement vector.

$$\mathbf{u} = \mathbf{u}_r + \mathbf{u}_d \quad \mathbf{u}_r = \mathbf{r}^{0n} - \mathbf{r}^0 \quad \mathbf{u}_d = \mathbf{r}^n - \mathbf{r}^{0n} \tag{7}$$

Introducing subscript  $c$  for the arithmetic mean of the coordinates of the points in the element, the position vectors in initial and shadow element configurations may be written as:

$$\begin{aligned} \mathbf{r}^0 &= \mathbf{r}_c^0 + \mathbf{x}^0 \\ \mathbf{r}^{0n} &= \mathbf{r}_c^{0n} + \mathbf{x}^{0n} = \mathbf{r}_c^0 + \mathbf{u}_c + \mathbf{R}_{0n} \mathbf{x}^0 \end{aligned} \tag{8}$$

where  $\mathbf{x}^0$  and  $\mathbf{x}^{0n}$  are the vectors from the centroid of the element to the point being considered in the  $C_0$  configuration and the  $C_{0n}$  configuration respectively. Substitution of the expressions above into Eq. (7) yields:

$$\mathbf{u}_d = \mathbf{u} - \mathbf{u}_r = \mathbf{u} - (\mathbf{r}^{0n} - \mathbf{r}^0) = \mathbf{u} - \mathbf{u}_c - (\mathbf{R}_{0n} - \mathbf{I})\mathbf{x}^0 \tag{9}$$

The rotation of an element node as it moves from the initial configuration  $C_0$  to the deformed configuration  $C_n$  is described by the rotation matrix  $\mathbf{R}$ . The rotation matrix is split into a rigid body rotation tensor  $\mathbf{R}_{0n}$  and a deformational rotation matrix  $\mathbf{R}_d$ .

$$\begin{aligned} \mathbf{R} &= \mathbf{R}_d \mathbf{R}_{0n} \\ \mathbf{R}_d &= \mathbf{R} \mathbf{R}_{0n}^T = \mathbf{R} \mathbf{T}_0^T \mathbf{T}_n \end{aligned} \tag{10, 11}$$

The deformational rotation matrix transformed into the local coordinate system shared by configurations  $C_{0n}$  and  $C_n$  reads

$$\tilde{\mathbf{R}}_d = \mathbf{T}_n \mathbf{R}_d \mathbf{T}_n^T = \mathbf{T}_n \mathbf{R} \mathbf{T}_0^T \tag{12}$$

The position of an element node  $a$  with initial coordinates  $r_a^0$ , is defined by the translational displacement  $u_a$  and the rotational orientation  $\mathbf{R}_a$ . Together, the set  $(u_a, \mathbf{R}_a)$  for  $a=1, \dots, N$  is the nodal displacement vector  $\hat{\mathbf{v}}$  “visible” to the other elements.  $\hat{\mathbf{v}}$  is interpreted as an array of numbers that defines the position of the deformed element. In order to establish the force vector and tangent stiffness for an element, the *deformational* vector for the element needs to be established. This vector is denoted  $\tilde{\mathbf{v}}_d$  and contains translational and rotational degrees of freedom for each element node ordered as

$$\tilde{\mathbf{v}}_d^T = [\tilde{\mathbf{u}}_{d1}^T \tilde{\boldsymbol{\theta}}_{d1}^T \dots \tilde{\mathbf{u}}_{dN}^T \tilde{\boldsymbol{\theta}}_{dN}^T] \quad (13)$$

$N$  is the number of element nodes for the element being considered.  $\tilde{\boldsymbol{\theta}}_d$  is obtained from  $\tilde{\mathbf{R}}_d$ .

### 3. Equilibrium and tangent stiffness

#### 3.1. Equilibrium

Balance in virtual work reads

$$\begin{aligned} \delta_R \tilde{\mathbf{v}}_d^T \tilde{\mathbf{f}}_e - \delta \mathbf{v}^T \mathbf{f}_{ext} &= \delta \mathbf{v}^T \left( \frac{\partial_R \mathbf{v}_d}{\partial \mathbf{v}} \right) \mathbf{T} \mathbf{f}_e - \mathbf{f}_{ext} = 0 \\ \Rightarrow \mathbf{f}_e &= \mathbf{T}^T \tilde{\mathbf{P}}^T \tilde{\mathbf{H}}^T \tilde{\mathbf{f}}_e = \mathbf{f}_{ext} \end{aligned} \quad (14)$$

The transformations are matrices that provide the large rotation effects, and are explained briefly in the following, see [12] for details. In the derivation we first need the variation of the transformation matrix with respect to infinitesimal rotations about the local coordinate axes:

$$\delta \mathbf{T}_n = \frac{\partial \mathbf{T}_n}{\partial \tilde{\omega}_i} \delta \tilde{\omega}_i = \begin{bmatrix} 0 & \delta \tilde{\omega}_z & -\delta \tilde{\omega}_y \\ -\delta \tilde{\omega}_z & 0 & \delta \tilde{\omega}_x \\ \delta \tilde{\omega}_y & -\delta \tilde{\omega}_x & 0 \end{bmatrix} \begin{bmatrix} \mathbf{i}_1^{nT} \\ \mathbf{i}_2^{nT} \\ \mathbf{i}_3^{nT} \end{bmatrix} = -\mathbf{Spin}(\delta \tilde{\omega}) \mathbf{T}_n \quad (15)$$

Transformation of  $\mathbf{Spin}(\delta \tilde{\omega})$  to global coordinates reads

$$\delta \mathbf{T}_n = -\mathbf{Spin}(\delta \tilde{\omega}) \mathbf{T}_n = -\mathbf{T}_n \mathbf{Spin}(\delta \omega) \mathbf{T}_n^T \mathbf{T}_n = -\mathbf{T}_n \mathbf{Spin}(\delta \omega) \quad (16)$$

$\mathbf{Spin}(\delta \omega)$  is anti-symmetric. Secondly, the rotation matrix  $\mathbf{R}_{0n}$  rotates a vector from initial configuration to the shadow configuration, hence the variation of the rotation matrix reads

$$\delta \mathbf{R}_{0n} = \delta \mathbf{T}_n^T \mathbf{T}_0 + \mathbf{T}_n^T \delta \mathbf{T}_0 = \delta \mathbf{T}_n^T \mathbf{T}_0 = \mathbf{Spin}(\delta \omega) \mathbf{T}_n^T \mathbf{T}_0 = \mathbf{Spin}(\delta \omega) \mathbf{R}_{0n} \quad (17)$$

The variation of a vector expressed in a global frame can be expressed as

$$\delta \mathbf{x} = \delta_{\mathbf{R}} \mathbf{x} + \delta \omega \times \mathbf{x} = \delta_{\mathbf{R}} \mathbf{x} + \mathbf{Spin}(\delta \omega) \mathbf{x} \quad (18)$$

where  $\delta_{\mathbf{R}} \mathbf{x}$  is the variation of the vector in the co-rotated frame, and  $\delta \omega$  is the variation of the global rotation of the frame. The variation of the *co-rotated* deformation

nal displacement vector  $\mathbf{u}_d$  in a co-rotated frame is obtained via the variation of the global deformational displacements with respect to global  $\mathbf{v}$ , and using Eq. (18) to find the variation of the co-rotated deformational *displacements* with respect to global  $\mathbf{v}$ . Eq. (9) states that deformational displacement of an element node  $a$  is

$$\mathbf{u}_{da} = \mathbf{u}_a - \mathbf{u}_c - (\mathbf{R}_{0n} - \mathbf{I})\mathbf{x}_a^0 = \sum_{b=1}^N \delta_{ab}\mathbf{u}_b - \sum_{b=1}^N \frac{1}{N}\mathbf{u}_b - (\mathbf{R}_{0n} - \mathbf{I})\mathbf{x}_a^0 \quad (19)$$

$\mathbf{u}_c$  is the displacement vector for the element centroid, and  $\delta_{ab}$  is the Kronecker delta, hence

$$\mathbf{u}_{da} = \sum_{b=1}^N \mathbf{P}_{ab}\mathbf{u}_b - (\mathbf{R}_{0n} - \mathbf{I})\mathbf{x}_a^0 \quad (20)$$

$$\mathbf{P}_{ab} = (\delta_{ab} - \frac{1}{N})\mathbf{I}$$

The variation of global  $\mathbf{u}_{da}$  with respect to global  $\mathbf{v}$  is found as

$$\delta\mathbf{u}_{da} = \sum_{b=1}^N \mathbf{P}_{ab}\delta\mathbf{u}_b - \delta\mathbf{R}_{0n}\mathbf{x}_a^0 \quad (21)$$

Using Eq. (17) we have

$$\delta\mathbf{R}_{0n}\mathbf{x}_a^0 = \mathbf{Spin}(\delta\omega_r)\mathbf{R}_{0n}\mathbf{x}_a^0 = \mathbf{Spin}(\delta\omega_r)\mathbf{x}_a^{0n} = -\mathbf{Spin}(\mathbf{x}_a^{0n})\delta\omega_r = -\mathbf{Spin}(\mathbf{x}_a^{0n})\mathbf{G}\delta\mathbf{v} \quad (22)$$

The matrix  $\mathbf{G}$  connects the variation of the rigid body rotation of the shell element to the variation of the visible node displacements:

$$\delta\omega_r = \frac{\partial\omega_r}{\partial v_i}\delta v_i = \mathbf{G}\delta\mathbf{v} = \sum_{b=1}^N \mathbf{G}_b\delta\mathbf{v}_b \quad (23)$$

The matrix  $\mathbf{G}$  is an element-type dependent matrix. The variation of *global*  $\mathbf{u}_d$  with respect to global  $\mathbf{v}$  then reads

$$\delta\mathbf{u}_{da} = \sum_{b=1}^N ([\mathbf{P}_{ab}0] + \mathbf{Spin}(\mathbf{x}_a^{0n})\mathbf{G}_b)\delta\mathbf{v}_b \quad (24)$$

$\delta_{vb}$  is the global degrees of freedom for node  $b$ . Using the relationship  $\mathbf{u}_{da} = \mathbf{x}_a^n - \mathbf{x}_a^{0n}$ , we find that the variation of the co-rotated deformational displacement vector with respect to global degrees of freedom is given by

$$\delta_R\mathbf{u}_{da} = \delta_R\mathbf{x}_a^n - \delta_R\mathbf{x}_a^{0n} = \delta_R\mathbf{x}_a^n \quad (25)$$

Since  $\mathbf{x}_a^n = \mathbf{R}_{0r} \mathbf{x}_a^0 + \mathbf{u}_{da}$ , the variation of global  $\mathbf{x}_a^n$  with respect to global degrees of freedom is given by

$$\delta \mathbf{x}_a^n = \delta \mathbf{R}_{0r} \mathbf{x}_a^0 + \mathbf{R}_{0r} \delta \mathbf{x}_a^0 + \delta \mathbf{u}_{da} = \sum_{b=1}^N \mathbf{P}_{ab} \delta \mathbf{u}_b \quad (26)$$

Substituting  $\mathbf{x}_a^n$  for  $\mathbf{x}$  in Eq. (18) and solving with respect to  $\delta_R \mathbf{x}_a^n$  yields

$$\begin{aligned} \delta_R \mathbf{x}_a^n &= \sum_{b=1}^N \mathbf{P}_{ab} \delta \mathbf{u}_b - \mathbf{Spin}(\delta \omega_r) \mathbf{x}_a^n = \sum_{b=1}^N \mathbf{P}_{ab} \delta \mathbf{u}_b + \mathbf{Spin}(\mathbf{x}_a^n) \delta \omega_r \\ &= \sum_{b=1}^N ([\mathbf{P}_{ab} \mathbf{0}] + \mathbf{Spin}(\mathbf{x}_a^n) \mathbf{G}_b) \delta \mathbf{v}_b \end{aligned} \quad (27)$$

Hence, we have the variation of co-rotated deformational displacement vector with respect to global degrees of freedom  $\delta_R \mathbf{u}_{da} = \delta_R \mathbf{x}_a^n$ .

By starting with the variation of the co-rotated deformational rotations with respect to global degrees of freedom, the variation of the co-rotated deformational (finite) rotations with respect to the co-rotated deformational (infinitesimal) rotations is obtained. The derivation is based on work by Nour-Omid and Rankin [15], and based on a relationship established by Simo [16] and Szwabowicz [17].

$$\delta_R \theta_{da} = \frac{\partial \theta_{da}}{\partial \omega_{da}} \delta_R \omega_{da} = \frac{\partial(\text{Axial}(\ln(\mathbf{R}_{da})))}{\partial \omega_{da}} \delta_R \omega_{da} = \mathbf{H}_a \delta_R \omega_{da} \quad (28)$$

$$\mathbf{H}_a = \frac{\partial \theta_a}{\partial \omega} = \mathbf{I} - \frac{1}{2} \mathbf{Spin}(\theta_a) + \eta \mathbf{Spin}(\theta_a)^2 \quad (29)$$

$$\eta = \frac{\sin \frac{1}{2} \theta_a - \frac{1}{2} \theta_a \cos(\frac{1}{2} \theta_a)}{\theta_a^2 \sin(\frac{1}{2} \theta_a)} \quad \text{and} \quad \theta_a = \sqrt{\theta_a^T \theta_a} = \|\theta_b\| \quad (30)$$

$$\delta_R \omega_{da} = \delta \omega_a - \delta \omega_r = \delta \omega_a - \frac{\partial \omega_r}{\partial v_i} \delta v_i = \delta \omega_a - \mathbf{G}_a \delta v_a \quad (31)$$

$\mathbf{G}$  is defined in Eq. (23).  $\delta_R \omega_{da}$  may now be written as

$$\delta_R \omega_{da} = \sum_{b=1}^N (\delta_{ab} [\mathbf{0} \ \mathbf{I}] - \mathbf{G}_b) \delta v_b \quad (32)$$

Introducing Eq. (31) into Eq. (28) yields the final expression for the variation of co-rotated deformational rotation with respect to global degrees of freedom.

$$\delta_R \boldsymbol{\theta}_{da} = \mathbf{H}_a \sum_{b=1}^N (\delta_{ab} [\mathbf{0} \quad \mathbf{I}] - \mathbf{G}_b) \delta v_b \quad (33)$$

277

For an element with  $N$  nodes, the nodal degrees of freedom are ordered as follows

278

$$\mathbf{v}^T = [\mathbf{u}_1^T \quad \boldsymbol{\theta}_1^T \quad \dots \quad \mathbf{u}_N^T \quad \boldsymbol{\theta}_N^T] \quad (34)$$

281

282

283

If Eqs. (27) and (33) are ordered accordingly,  $\delta_{Rv_d}$  (containing both displacements and rotations) may be written as

285

$$\delta_{Rv_d} = \mathbf{H}(\mathbf{I} - \mathbf{P}_T - \mathbf{P}_R) \delta v = \mathbf{H}\mathbf{P} \delta v \quad (35)$$

286

287

288

Matrix  $\mathbf{P}$  is a nonlinear projector operator that filters out rigid body translation and rotation.

289

290

291

292

The variation of the co-rotated deformational displacement vector has now been found with respect to a set of global degrees of freedom. To enable use of existing linear elements put in the rotating frame, the global system is chosen to be that of the co-rotated element. Thus, Eq. (34) is modified to

293

$$\delta_{R\tilde{v}_d} = \tilde{\mathbf{H}}\tilde{\mathbf{P}}\delta\tilde{v} \quad (36)$$

295

296

297

298

Since the visible degrees of freedom are defined in the global coordinate system, the variation needed is  $\delta_{Rv_d}$  with respect to  $\delta v$ . Taking advantage of the transformation between local and global coordinate system, we have

299

$$\delta_{R\tilde{v}_d} = \tilde{\mathbf{H}}\tilde{\mathbf{P}}\mathbf{T}_n \delta v \quad (37)$$

301

302

### 3.2. Tangent stiffness

303

304

The consistent tangent stiffness is obtained by the variation of the internal force vector  $f_e$  with respect to the visible degrees of freedom,  $v$ :

305

306

$$\delta f_e = \frac{\partial f}{\partial v} \delta v = \mathbf{K}_t \delta v \quad (38)$$

307

308

Using Eq. (14) for  $f_e$ , Eq. (38) yields:

309

$$\begin{aligned} \delta f &= \delta \mathbf{T}^T \tilde{\mathbf{P}}^T \tilde{\mathbf{H}}^T \tilde{f}_e + \mathbf{T}^T \delta_R \tilde{\mathbf{P}}^T \tilde{\mathbf{H}}^T \tilde{f}_e + \mathbf{T}^T \tilde{\mathbf{P}}^T \delta_R \tilde{\mathbf{H}}^T \tilde{f}_e + \mathbf{T}^T \tilde{\mathbf{P}}^T \tilde{\mathbf{H}}^T \delta \tilde{f}_e \\ &= (\mathbf{K}_{GR} + \mathbf{K}_{GP} + \mathbf{K}_{GM} + \mathbf{K}_{MG}) \delta v = \mathbf{K}_T \delta v \end{aligned} \quad (39)$$

312

313

The different terms of the tangent stiffness represent rotational geometric stiffness,

projection geometric stiffness, moment correction geometric stiffness, and material stiffness, respectively.

The rotational geometric stiffness arises from the variation of the transformation matrix between initial configuration  $C_0$  and shadow configuration  $C_n$ . As a rigid rotation of a stressed element rotates the stresses, the internal forces change direction to preserve equilibrium.

The equilibrium projection geometric stiffness arises from the variation of the projector matrix  $\tilde{\mathbf{P}}^T$ , and reflects the variation of the force vector due to variations in the degrees of freedom.

The moment correction geometric stiffness arises from variation of the rotation pseudo-vector Jacobian  $\tilde{\mathbf{H}}$ .

The following expression for the consistent tangent stiffness is determined:

$$\mathbf{K}_t = \mathbf{T}^T (\tilde{\mathbf{K}}_{MG} + \tilde{\mathbf{K}}_{GM} + \tilde{\mathbf{K}}_{GR} + \tilde{\mathbf{K}}_{GP}) \mathbf{T} = \mathbf{T}^T (\tilde{\mathbf{P}}^T \tilde{\mathbf{H}}^T \tilde{\mathbf{K}}_e \tilde{\mathbf{H}} \tilde{\mathbf{P}} + \tilde{\mathbf{P}}^T \tilde{\mathbf{M}} \tilde{\mathbf{P}} - \tilde{\mathbf{F}}_{nm} \tilde{\mathbf{G}} - \tilde{\mathbf{G}}^T \tilde{\mathbf{F}}_n^T \tilde{\mathbf{P}}) \mathbf{T} \quad (40)$$

It should be noted that for linear geometry analysis, only  $\tilde{\mathbf{K}}_e$  remains. A detailed derivation of above relationships is given in [6,12].

### 3.3. Elastic-plastic stiffness

$\tilde{\mathbf{K}}_e$  represents the material stiffness for the element, and may include plasticity effects. It connects the local deformational dof increment with the local force increment:

$$\delta \tilde{\mathbf{f}}_e = \tilde{\mathbf{K}}_e \delta_R \tilde{\mathbf{v}}_d \quad (41)$$

The linear version of Ilyushin's stress resultant yield condition may be written

$$f(\tilde{\mathbf{n}}, \tilde{\mathbf{m}}) = \sqrt{\left( \frac{\tilde{N}}{t^2} + \frac{4s\tilde{P}}{\sqrt{3}t^3} + \frac{16\tilde{M}}{t^4} \right)} - \sigma_0 = 0 \quad (42)$$

$$\tilde{N} = N_x^2 + N_y^2 - N_x N_y + 3N_{xy}^2$$

$$\tilde{M} = M_x^2 + M_y^2 - M_x M_y + 3M_{xy}^2$$

$$\tilde{P} = N_x M_x + N_y M_y - 0.5N_x M_y - 0.5N_y M_x + 3N_{xy} M_{xy}$$

$$s = \tilde{P} / \text{abs}(\tilde{P}) = \pm 1$$

For thin shells of Mises material this criterion works well. Denoting the integration point stress resultant vector by  $\boldsymbol{\sigma} = [\tilde{\mathbf{n}}, \tilde{\mathbf{m}}]^T$  the yield criterion is rewritten in quadratic form, see Ibrahimbegovic and Frey [17] and Matthies [18]:

$$f = \boldsymbol{\sigma}^T \mathbf{A} \boldsymbol{\sigma} - \left(1 + \frac{H\epsilon_p}{\sigma_y}\right)^2 = 0 \quad (43)$$

$$A = \begin{bmatrix} \frac{1}{n_0^2} \bar{A} & \frac{s}{2\sqrt{3}m_0 n_0} \bar{A} \\ \frac{s}{2\sqrt{3}m_0 n_0} \bar{A} & \frac{1}{m_0^2} \bar{A} \end{bmatrix} \quad \bar{A} = \begin{bmatrix} 1 & -0.5 & 0 \\ -0.5 & 1 & 0 \\ 0 & 0 & 3 \end{bmatrix}$$

356

357

359

$$m_0 = 0.25\sigma_y t^2, n_0 = \sigma_y t$$

360

361

362

363

364

365

The off-diagonal submatrices in  $A$  lead to corners in the yield surface [19–21]. Assuming  $s=0$ , a hyperellipse is obtained as yield surface. This leads to nonconservative inaccuracies. The maximum error is approximately 12% for balanced membrane and bending loading. Approaching each axis, the error vanishes. Utilising an associated flow rule, the backward Euler update of the plastic strain increment reads

366

367

$$\Delta \epsilon_{p,n+1} = \Delta \lambda_{n+1} \frac{\partial f}{\partial \sigma_{n+1}} \Delta \epsilon = [\Delta \epsilon_m, \Delta \kappa]^T \quad (44)$$

368

369

370

371

Here  $n+1$  corresponds to the current load step in the global Newton–Raphson equilibrium iteration. A linear isotropic work hardening model is used:

372

$$\sigma^T d\epsilon = \bar{\sigma} d\epsilon_p \Rightarrow d\epsilon_p = 2\bar{\sigma} d\lambda \quad \bar{\sigma} = \sqrt{\sigma^T A \sigma} \quad (45)$$

373

374

375

In the elastic predictor plastic corrector approach applied herein, the stress update is obtained by

376

$$\sigma_{n+1} = \sigma_{\text{trial}} - C \Delta \epsilon_{p,n+1} = \bar{Q}^{-1} \sigma_{\text{trial}} \quad \bar{Q} = [I + 2\Delta \lambda CA]$$

377

378

379

$$C = \begin{bmatrix} tD & 0 \\ 0 & \frac{t^3}{12} D \end{bmatrix} \quad D = \frac{E}{1-\nu^2} \begin{bmatrix} 1 & \nu & 0 \\ \nu & 1 & 0 \\ 0 & 0 & \frac{1-\nu}{2} \end{bmatrix}$$

380

381

382

383

The discrete yield condition  $f_{n+1}$  now depends only on  $\Delta \lambda$ . Solving for  $f(\Delta \lambda_{n+1})$  (Newton–Raphson) the stress update is directly obtained. The consistent material tangent for an integration point in the plane reads:

384

385

$$d\sigma = \left[ H - \frac{H g g^T H}{g^T H g + \beta} \right] d\epsilon = C_t d\epsilon \quad (46)$$

386

$$H^{-1} = C^{-1} + 2\Delta \lambda A, \quad g = 2A\sigma$$

388

1  
2  
3  
389

### 3.4. Shell element and solution procedure

390 Triangular facet finite elements with six dof at each node is employed. The pro-  
391 cedure for construction of the stiffness is presented by Militello and Felippa [9]. The  
392 element stiffness is split into a basic and higher order contribution. The basic stiffness  
393 is derived from a constant stress in the element doing virtual work on element bound-  
394 ary displacements described in terms of the visible degrees of freedom:

$$395 \quad \mathbf{K}\mathbf{v}=(\mathbf{K}_b+\mathbf{K}_h)\mathbf{v}=\mathbf{f} \quad (47)$$

397  
398 With this approach, the individual element (patch) test is satisfied. The higher  
399 order stiffness is derived by means assumed natural deviatoric strains (ANDES),  
400 with local (invisible) dof for bending from element curvature interpolation and from  
401 the drilling dof for the membrane part.

402 The balance equation between internal and external forces for the assembled  
403 element model reads

$$404 \quad r(\mathbf{v},\lambda)=f(\mathbf{v})-p(\lambda)=0 \quad (48)$$

406  
407 The external loads are hence written as a function of a time like parameter  $\lambda$ .  
408 Advancing from state  $n$  to  $n+1$  is carried out by means of a corresponding load  
409 increment followed by Newton–Rapshon iterations on the residual, with the orthog-  
410 onal trajectory method by Fried [22] employed in order to traverse limit points.

411 The update of the global displacement and rotation is obtained as follows displace-  
412 ments:

$$413 \quad \text{displacements: } \mathbf{v}:=\mathbf{v}+\Delta\mathbf{v} \quad (49)$$

$$416 \quad \text{rotations: } \mathbf{R}:=\mathbf{R}(\Delta\omega)\mathbf{R} \quad (50)$$

417

## 418 4. Numerical simulations

419 In the following, some cases are analysed in order to investigate accuracy of the  
420 simplified plasticity model. Cases with loading dominated by either membrane or  
421 bending conditions should be accurate, whereas cases with combined load carrying  
422 may be nonconservative. Other numerical studies with the present formulation may  
423 be found in [11,12].

### 424 4.1. Three-point bending of plates

#### 425 4.1.1. Steel material

426 A rectangular steel plate of elastic-perfectly plastic material with yield stress 400  
427 MPa is analysed with two different sets of boundary conditions. The first set has

1

428  
429  
430  
431  
432  
433  
434  
435  
436  
437  
438  
439  
440

displacement restraints on two opposite edges (the two other unrestrained). This boundary condition promotes a nonlinear membrane force effects in the plate as the out-of-plane deflection increases. The other boundary set has axially free motion at two opposite edges, the rest of the boundary conditions are as described above. With this latter boundary, the load is carried by dominating bending moments. A line load at midplate is applied, hence a three-point bending load system is obtained. The plate was analysed with an in-house program Cfem [6,12] and ABAQUS. Cfem employs the stress resultant plasticity model and the kinematical description given in above sections, whereas ABAQUS employs through thickness stress integration, i.e. a layer approach. With this one obtains comparison between the two plasticity models and two different descriptions of nonlinear geometry effects. An additional feature with ABAQUS is that the account of large deformation can be easily switched off, i.e. having a linear geometry description.

441  
442  
443  
444  
445  
446  
447

Fig. 2a illustrates the two simulations for axially fixed boundary conditions. For this thin plate (2000×750×50 mm, i.e.  $L/t=40$ ) a strong membrane force evolves. There is a transition region where the two simulations deviates slightly, but the overall correspondence is very good. Fig. 2b depicts the simulations for axially unrestrained boundary conditions. Due to not accounting for first fibre yielding with the stress resultant model there is a small deviation in the elastic-plastic transition, elsewhere the correspondence is very good.

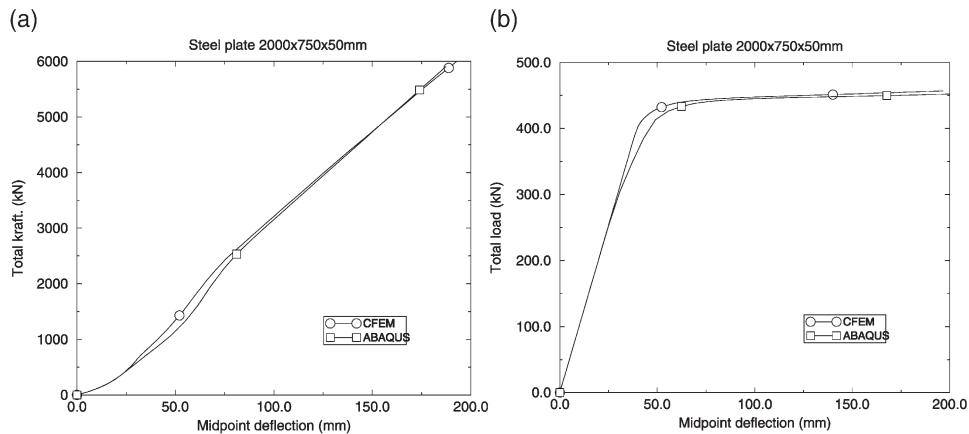
448

#### 4.1.2. Aluminium materials

449  
450  
451  
452  
453  
454

In the steel material simulations the stress-strain curve is assumed to be bilinear. In order to investigate how the stress resultant modelling performs for nonlinear stress strain curves, an aluminium alloy (Al 2024) of tempers  $T_3$  and  $T_4$  was analysed. The stress strain curves are plotted in Fig. 3. The linear hardening simplification for the stress resultant model is indicated. Exactly the same geometry and boundary conditions as employed for the steel plate are used here.

13



14  
15

Fig. 2. Steel plate in three-point bending. (a) In-plane restrained plate, (b) in-plane unrestrained plate.

1

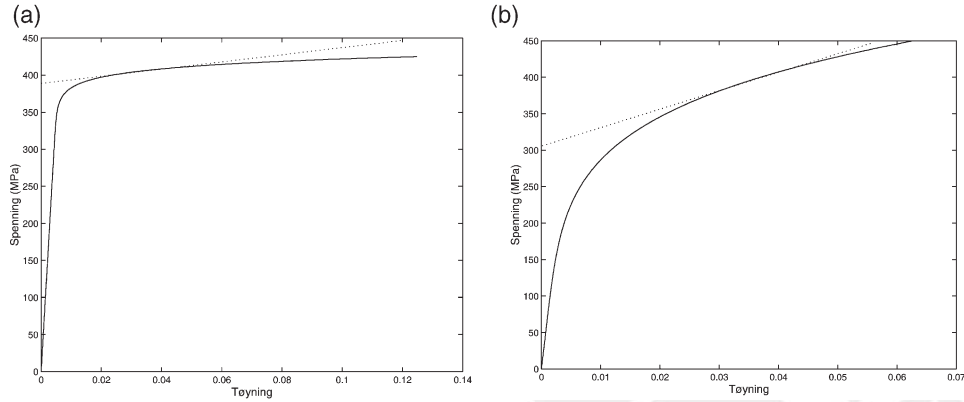


Fig. 3. Stress–strain curves for aluminium 2024. (a) Temper T3, (b) temper T4.

For the axially fixed boundary conditions Fig. 4a shows good correspondence between the two formulations. There is, however, a small difference for large rotations, at deflections above 250 mm the plate has rotated approximately 14 degrees (0.24 rad). This is a large rotation for this problem. Hence, due to some difference in treating large rotations in the two programs, some deviation occurs. Fig. 4b shows the simulations for axially free boundary conditions. A larger difference in the region of gradual thickness plastification as compared to the steel material appears, but the two simulations accounting for large rotations correspond well. Interestingly, running the same problem assuming a linear geometry formulation, one observes that a large rotation effect is already present in the plate for a deflection of 150 mm (comparing with the simulations accounting for this). Hence, assuming a linear formulation leads to a conservative limit load in this bending dominated case.

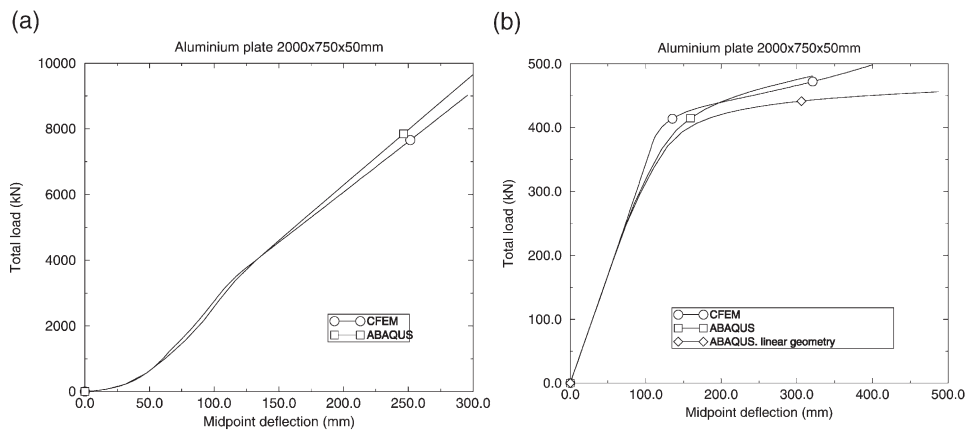


Fig. 4. Aluminium (T3) plate in three-point bending. (a) In-plane restrained plate, (b) in-plane unrestrained plate.

Turning to the  $T_4$  temper, a very nonlinear stress strain curve must be used. Fig. 5a shows that the difference between the two simulations is larger than for the  $T_3$  material. However, the overall correspondence for this boundary condition is acceptable. For a bending dominated load carrying (Fig. 5b), the difference is significant. Here the effect of the simplified bilinear hardening model for the stress resultant plasticity combined with not accounting for gradual plastification over thickness is accentuated. Hence, for such stress strain curves the stress resultant hardening model must be improved. The linear geometry analysis shows the same conservative response as for the  $T_3$  material.

#### 4.2. Steel plate in compression

A quadratic steel plate of same material as in above subsection is subjected to compression on two opposite edges. The corresponding edges are constrained to have the same axial displacement. The length to thickness ratio is 100. All edges are free to rotate around the axes parallel to the boundaries, with free in-plane displacements, but fixed with respect to out-of-plane deflection. A half-wave sine imperfection is employed with amplitude of 2 mm (0.1 thickness). Fig. 6 shows the comparison between the stress resultant modelling approach and ABAQUS. A significant overprediction is obtained. This may partially explained by Fig. 7b that shows a plot of the simplified yield surface employed herein and the correct linear Ilyushin yield criterion. For a balanced membrane and bending situation the error is at its largest. Fig. 7a depicts the evolution of the out-of-plane deflection at plate center point. At collapse it is of magnitude 15 mm. Assuming a sinusoidal deflection shape, an average central deflection is calculated to be 4.1 mm. This gives a corresponding average bending moment along the midplate that locates the membrane and bending situation as illustrated in Fig. 7b. Hence, the deviation should be at its maximum. Taking the yield stress to be 0.88 of the nominal value (i.e. 352 MPa), the simulation given in Fig. 6 shows acceptable correspondence to the more detailed simulation. This shows

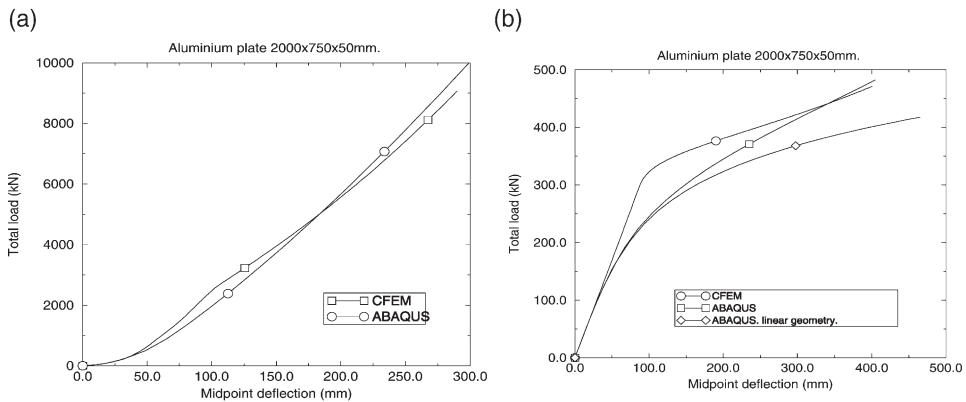


Fig. 5. Aluminium ( $T_4$ ) plate in three-point bending. (a) In-plane restrained plate, (b) in-plane unrestrained plate.

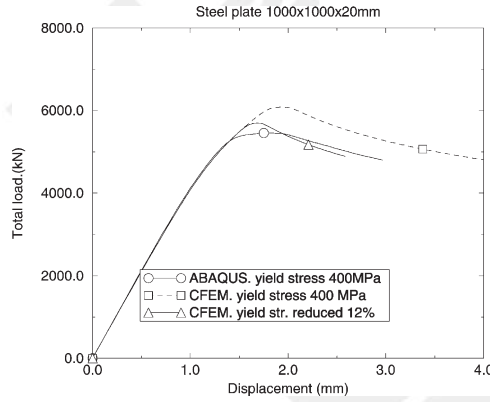
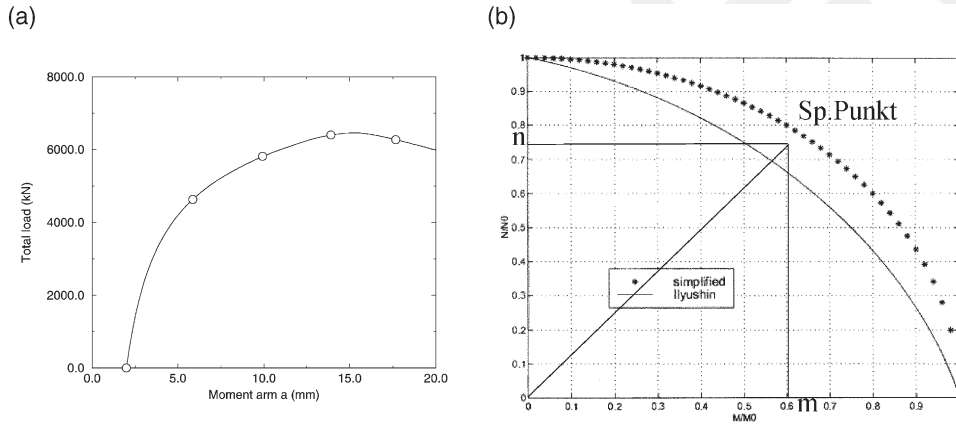


Fig. 6. Steel plate in compression.

39  
40  
41

42



3  
2

45  
46  
47  
48

Fig. 7. Steel plate in compression. (a) Out-of-plane plate deflection, (b) yield surfaces and combination of membrane and bending of compressed plate.

494 that a pragmatic correction of yield stress may provide reasonable limit load values  
495 for plates in compression. One may also assume directly such a reduced yield stress,  
496 and employ this in screening analyses of compressed plates.

497 *4.3. Torsion of a plate with a central hole*

498 The present case was first presented by Basar and Itskov [24], and Itskov [25].  
499 A rectangular plate is fully constrained with respect to in-plane displacement at two  
500 opposite edges (the two other edges are free). Then one end of the plate is subjected  
501 to a large torsional rotation. The material data employed is yield stress 0.2 and linear  
502 hardening 3.0. The geometry is  $5 \times 1 \times 0.05$ . A circular hole is located at plate center  
503 point. Since the plate can not contract due to the boundary conditions, a large mem-

1

1  
2  
3  
504  
505  
506  
507  
508  
509  
510  
511  
512  
513

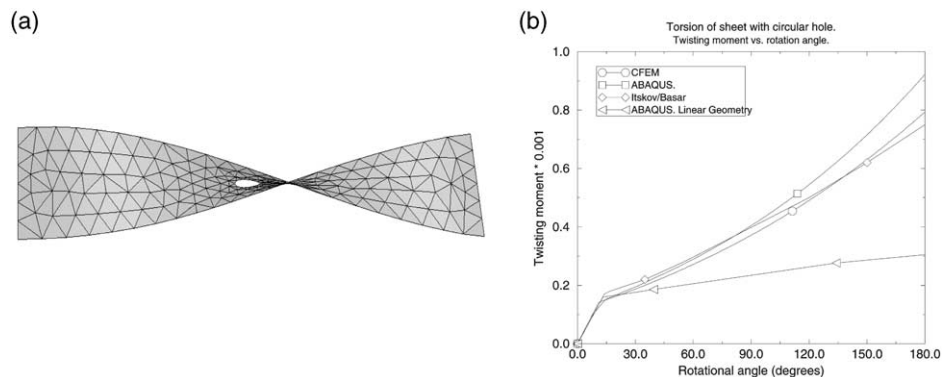
brane force will develop for increasing rotation. Fig. 8a shows the deformed mesh for a rotation of 180 degrees. Fig. 8b shows the corresponding applied end rotation and corresponding torsion moment. The agreement between the present simulation and the one by Basar and Itskov is very good. These two simulations disagree somewhat with the ABAQUS simulation for rotations larger than about 90 degrees. This stems from different nonlinear geometry formulations. Running the simulation with the linear geometry option, one observes the significant effect of large rotations. The simulation becomes much too soft. Up to about 20 degrees, however, the simulations agree quite well. So for this case one may say that above this value one has large rotation effects.

514 4.4. Shear buckling of plate girders

515 The following simulations are compared to the test results determined by Tang  
516 and Evans [26]. They tested steel plate girders with/without longitudinal stiffeners.  
517 The test specimens were of type three-point bending. Figs. 10 and 11 show the  
518 geometry of deformed specimens and corresponding simulated shapes. The steel has  
519 approximately 200 MPa yield strength, but this differs between web, flange, and  
520 stiffener (accounted for in the simulations). Confer [26] for details. Furthermore, the  
521 girder length is 2.4 m, height 0.6 m, and web thickness 2.5 mm. Hence, the length  
522 to thickness ratio for an unstiffened web panel is about 385.

523 Fig. 9a illustrates the total load versus midpoint deflection of the girder for the  
524 test and the two simulations. The case is the unstiffened girder. Some deviation in  
525 elastic initial stiffness is observed. This is very typical when comparing numerical  
526 simulations with tests; the boundary conditions in the test are usually difficult to  
527 achieve exactly in the numerical models. The limit load and post-collapse behaviour  
528 is considered most interesting here. The ABAQUS simulation diverged prematurely.  
529 The stress resultant approach simulation corresponds quite well to the test result,

50  
51



52  
53  
54  
55

Fig. 8. Large torsion rotation of steel plate with a hole. (a) Deformed mesh at 180 degrees end rotation, (b) response.

1

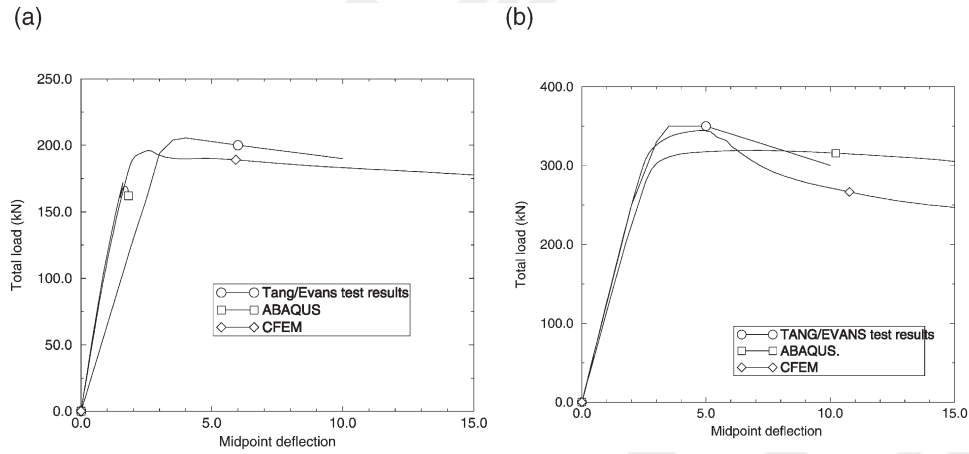


Fig. 9. Shear buckling response of steel girders. (a) Unstiffened girder, (b) stiffened girder.

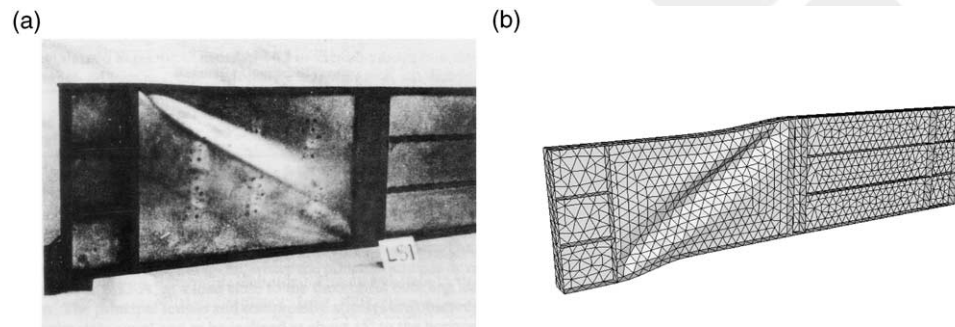


Fig. 10. Deformed unstiffened girder. (a) Test, (b) simulation.

both with respect to limit load and post-collapse behaviour. Comparing the figures in Fig. 10, the buckle shape is very well predicted.

Considering the stiffened girder (Fig. 11), Fig. 9b gives the test result and simulations. Interestingly, the present formulation captures the correct (unsymmetric) col-

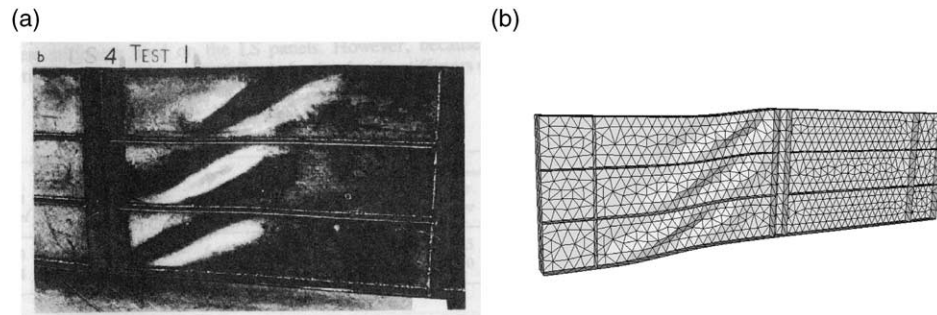


Fig. 11. Deformed stiffened girder. (a) Test, (b) simulation.

1  
2  
3  
534  
535  
536  
537  
538  
539  
  
540  
  
541  
542  
543  
544  
545  
546  
547  
548  
549  
550  
551  
552  
553  
554  
555  
556  
557  
558  
559  
560  
561  
562  
563  
564  
565  
566  
567  
568  
569  
570  
571  
572  
573  
574  
575

lapse shape, whereas ABAQUS reaches a symmetric collapse mode. This is the reason for the deviation between ABAQUS simulation and test (Fig. 9b). The present formulation yields good correspondence with the test. It should be noted that exactly the same finite element mesh, boundary conditions, and loading were employed in the two simulations. Fig. 11 shows again that the predicted collapse mode agrees well with the observed one.

### 5. Concluding remarks

The present investigation gives further insight into the performance of simplified plasticity modelling by means of stress resultants combined with high-performance thin shell finite elements. For materials with a relatively sharp transition from elastic to plastic behaviour and close to linear hardening, the simplified model works well. For hardening behaviour as exemplified by the T4 temper aluminium alloy, a refined hardening model must be used in order to obtain reliable results. The response of structures that have a gradual spread of plasticity (in the plane) seems to be simulated with acceptable accuracy. In inelastic buckling of plates the lack of modelling gradual plastification over thickness gives one source of inaccuracy. The non-conservatism in the stress resultant yield surface employed herein gives another. This may, however, be accounted for by using a reduced yield stress accounting for the inaccuracy for combined membrane and bending conditions. If a simplified plasticity model is employed for compression loaded components and structures of critical importance, the simulations should be supplemented with simulations accounting for gradual plastification over thickness.

The importance of correct account of terms giving nonlinear geometry stiffness was pointed out by comparison with simulations based on a linear geometry formulation. The nonlinear membrane force contribution in tension loaded shells was illustrated. For plates loaded in bending, the large rotations were of importance for rather small deflections, but assuming a linear geometry formulation provided conservative response. In compression loading the nonlinear geometry of course must be accounted for. The simulations also show that rotation magnitudes to be considered large differ significantly for different problems.

The ability of the present formulation to simulate the buckling modes in shear buckling of plate girders with/without longitudinal stiffeners was very good. For a symmetric structure the present formulation also captured the unsymmetric mode observed in the test. There is a small unsymmetry in the central part of the finite element mesh that may trigger this, but another formulation in a commercial program using the same mesh triggered a symmetric mode.

Herein, focus has been on planar shell structures. Curved shells are analysed in [11,12], showing acceptable prediction of response by the modelling presented above. In conclusion, one may state that stress resultant plasticity modelling of thin shells combined with a good description of nonlinear geometry (employing a consistent tangent stiffness) yields efficient computations for shell problems, both in structures subjected to dominating bending, compression, tension, and combinations. In com-

pression, however, the results may be taken as initial results as a basis for screening and importance studies. Furthermore, if there are large uncertainties related to the loads/boundary conditions/material properties/structural geometry, the simplified material model has a model bias that may be acceptable in the overall perspective.

## 6. Uncited reference

[23]

## References

- [1] Wempner GA. Finite elements, finite rotations and small strains of flexible shells. *Int J Solids Struct* 1969;5:117–53.
- [2] Rankin CC, Brogan FA. An element-independent corotational procedure for the treatment of large rotations. *ASME J Pressure Vessel Technol* 1986;108:165–74.
- [3] Rankin CC, Nour-Omid B. The use of projectors to improve finite element performance. *Computers and Struct* 1988;30:257–67.
- [4] Szwabowicz ML. Variational formulation in the geometrically non-linear thin elastic shell theory. *Int J Solids Struct* 1986;22:1161–75.
- [5] Bergan PG, Nygård MK. Nonlinear shell analysis using free formulation finite elements. In: *Finite element methods for nonlinear problems*, Berlin: Springer Verlag, 1989:317–338.
- [6] Haugen B. Buckling and stability problems for thin shell structures using high performance finite elements. Ph.D thesis, Univ. Colorado, Dept. Aerospace Engng, 1994.
- [7] Felippa CA, Militello C. Membrane triangles with corner drilling freedoms: II. The ANDES element. *Finite Elements in Anal and Des* 1992;12:189–201.
- [8] Felippa CA, Alexander S. Membrane triangles with corner drilling freedoms: III. Implementation and performance evaluation. *Finite Elements in Anal and Des* 1992;12:203–39.
- [9] Bergan PG, Hanssen L. A new approach for deriving “good” finite elements. MAFELAP II Conference, Brunel University, 1975. In: Whiteman JR, editor. *The Mathematics of Finite Elements and Applications*, vol. II. London: Academic Press, 1976:483–97.
- [10] Skallerud B. Efficient stress resultant plasticity formulations for thin shell applications: Implementation and numerical tests. SINTEF report STF22 F9671, 1998.
- [11] Skallerud B, Haugen B. Simplified stress resultant plasticity modelling in collapse analysis of thin shells. In: Wunderlich W, editor. *1. European Conference on Computational Mechanics ECCM’99 CD-ROM*, Munchen, 1999.
- [12] Skallerud B, Haugen B. Collapse of thin shell structures — stress resultant plasticity modelling within a co-rotated ANDES finite element formulation. *Int J Numerical Meth Engng* 1999;36:1961–86.
- [13] Masoaka K, Okada H, Ueda Y. A rectangular plate element for ultimate strength analysis. In: Shanmugan NE, Liew JYR, Thevendran V, editors. *Thin-walled structures*. Singapore: Elsevier, 1998:469–77.
- [14] Argyris JH. An excursion into large rotations. *Comput Methods Appl Mech Engng* 1985;32:85–155.
- [15] Nour-Omid B, Rankin CC. Finite rotation analysis and consistent linearization using projectors. *Comput Methods App Mech* 1991;93:353–84.
- [16] Simo JC. A finite strain beam formulation. The tree dimensional dynamic problem. Part I. *Comput Methods Appl Mech Engng* 1985;49:55–70.
- [17] Ibrahimbegovic A, Frey F. Stress resultant elasto-plastic analysis of plates and shallow shells. *COMPLAS-3*, Barcelona, 1992;2047–2059.

1  
2  
3  
620  
621  
622  
623  
624  
625  
626  
627  
628  
629  
630  
631  
632  
633  
634  
635  
636

[18] Matthies H. A decomposition method for integration of elastic–plastic rate problem. *Int J Numerical Meth Engng* 1989;28:1–11.

[19] Simo JC, Kennedy JG. On a stress resultant geometrically exact shell model. Part V Nonlinear plasticity: formulation and integration algorithm. *Comp Meth Applied Mech Engng* 1992;96:133–71.

[20] Crisfield M, Peng X. Efficient nonlinear shell formulation with large rotations and plasticity. *COMPLAS-3*, Barcelona, 1992, 1979–1997.

[21] Simo JC, Kennedy JG, Govindjee S. Non-smooth multisurface plasticity and viscoplasticity. Loading/unloading conditions and numerical algorithms. *Int J Numerical Meth Engng* 1988;26:2161–85.

[22] Fried I. Orthogonal trajectory accession on the nonlinear equilibrium curve. *Comput Meth Appl Mech Engng* 1984;47:283–97.

[23] Hibbit, Karlson, and Sorenson. *Abaqus manuals*.

[24] Basar Y, Itskov M. Constitutive model and finite element formulation for large strain elasto–plastic analysis of shells. *Comput Mech* 1999;23:466–81.

[25] Itskov M. Personal communication. 2000.

[26] Tang KH, Evans HR. Transverse stiffeners for plate girder webs — and experimental study. *J. Construct. Steel Research*, 1984.

3  
2